TECHNIQUE REPORT
SOLID EARTH: MARINE GEOPHYSICS

Earth and Planetary Physics
7: 582–602, 2023
doi: 10.26464/epp2023073

Seismic monitoring of sub-seafloor fluid processes in the Haima cold seep area using an Ocean Bottom Seismometer (OBS)

Bin Liu[1,2*], JianYu Huang[1,2], WenBin Jiang[1,3], WeiWei Wang[1,2], and Li Yang[1,3]

[1]Guangzhou Marine Geological Survey, Guangzhou 511458, China;

[2]Southern Marine Science and Engineering Guangdong Laboratory (Guangzhou), Guangzhou 511458, China;

[3]National Engineering Research Center for Gas Hydrate Exploration and Development, Guangzhou 511458, China

Key Points:

- An ocean bottom seismometer consisting of three orthogonal geophones and a hydrophone was used to monitor the sub-seafloor fluid process in a cold seep area.
- These data are analyzed in this first report of short duration events that are linked with sub-seafloor fluid migration in the South China Sea.
- A better understanding of the activity of the Haima cold seep is achieved.

Citation: Liu, B., Huang, J. Y., Jiang, W. B., Wang, W. W., and Yang, L. (2023). Seismic monitoring of sub-seafloor fluid processes in the Haima cold seep area using an Ocean Bottom Seismometer (OBS). *Earth Planet. Phys.*, *7*(5), 582–602. http://doi.org/10.26464/epp2023073

Abstract: The use of ocean bottom seismometers provides an effective means of studying the process and the dynamic of cold seeps by continuously recording micro-events produced by sub-seafloor fluid migration. We deployed a four-component Ocean Bottom Seismometer (OBS) at an active site of the Haima cold seep from 6 November to 19 November in 2021. Here, we present the results of this short-term OBS monitoring. We first examine the OBS record manually to distinguish (by their distinctive seismographic signatures) four types of events: shipping noises, vibrations from our remotely operated vehicle (ROV) operations, local earthquakes, and short duration events (SDEs). Only the SDEs are further discussed in this work. Such SDEs are similar to those observed in other sea areas and are interpreted to be correlated with sub-seafloor fluid migration. In the OBS data collected during the 14-day monitoring period. We identify five SDEs. Compared to the SDE occurrence rate observed in other cold seep regions, five events is rather low, from which it could be inferred that fluid migration, and subsequent gas seepage, is not very active at the Haima site. This conclusion agrees with multi-beam and chemical observations at that site. Our observations thus provide further constraint on the seepage activity in this location. This is the first time that cold seep-related SDEs have been identified in the South China Sea, expanding the list of sea areas where SDEs are now linked to cold seep fluid migration.

Keywords: cold seep; OBS (Ocean Bottom Seismometer); SDE (short duration event); Haima; South China Sea

1. Introduction

Methane seepage from sub-seafloor sediments into the water column is very common in the ocean (Judd, 2003). Areas of ocean floor where methane seepage occurs are termed cold seeps. The released methane may cause ocean acidification (Suess, 2014). A rough estimation has concluded shown that 6.6–19.5 Tg of methane per year are released into the atmosphere from the marine environment (Judd et al., 2002). Because methane is a more potent greenhouse gas than CO_2, some researchers have been concerned that this source of methane may accelerate global climate warming (Marín-Moreno et al., 2013; Myhre et al. 2016). From the perspective of resource exploration, methane seepage often is connected to gas hydrates, which have great potential as a novel energy source. In summary, methane seepage attracts considerable attention in both scientific and industrial communities.

The process of methane seepage has been studied using a wide variety of approaches, including hydro-acoustic, geo-chemical, and geophysical techniques. Cold seeps are often found by hydroacoustic methods, such as analyzing high-frequency acoustic water column data to spot anomalies that frequently take the form of flares (Greinert et al., 2006; Westbrook et al., 2009; Brothers et al., 2014; Römer et al., 2014). The geochemical method is widely used to study the life cycle and the origin of the methane by analyzing the chemo-synthetic biotics, authigenic carbonate, and pore fluid associated with cold seeps (Bayon et al., 2015; Feng D and Chen DF, 2015; Chen F et al., 2016; Crémière et al., 2016; Li N et al., 2016; Franchi et al., 2017; Liang QY et al., 2017). Geophysical methods are used to study the subsurface structures beneath seepage sites. 2D/3D multi-channel seismic methods provide images of subsurface structures beneath cold seeps from the

Correspondence to: B. Liu, liugele@163.com
Received 18 APR 2023; Accepted 30 JUN 2023.
First Published online 11 AUG 2023.

deep to the shallow (Riedel et al., 2002, 2006; He T et al., 2009; Crutchley et al., 2010; Sarkar et al., 2012; Hsu et al., 2018; Liu B et al., 2021a). High-frequency sub-bottom profilers provide very detailed images of near-seafloor structures (Riedel et al., 2002, 2006). Recently, the controlled source electromagnetics (CSEM) method has been used to study the internal structure of cold seeps (Goswami et al., 2015, 2016; Attias et al., 2016). Based on subsurface structure images, the location of a methane source and how its methane migrates from the deep to the seafloor can be inferred.

However, dynamic aspects of the cold seep process remain unclear due to a lack of monitoring. The temporal variation of a seepage may be deduced using time-lapse geophysical surveys (Riedel, 2007; Bangs et al., 2011), but that approach is quite costly and frequently takes a long time. Recently, ocean bottom seismometers (OBSs) have been used to study the cold seep process. An OBS is typically used in marine settings to monitor natural earthquakes and long duration events related to the volcano process. More and more experiments show that OBS data provide effective additional ways to study the sub-seafloor fluid process (Tary et al., 2012; Batsi et al., 2019). OBS data make it possible not only to track the temporal variation of a cold seep's activity but also to learn how fluids migrate through the system.

When an OBS is used to monitor sub-seafloor fluid processes, short duration events (SDEs) are commonly recorded (Tary et al., 2012; Tsang-Hin-Sun et al., 2019; Batsi et al., 2019; Domel et al., 2022). SDEs are so-named because of their abrupt onset and conclusion (usually within < 1 s); they have been reported in many sea areas, such as in the Marmara (Tary et al., 2012) and in the Svalbard (Franek et al., 2017; Domel et al., 2022). SDEs are believed to be strongly linked to fluid migration events, a potentially important advance in our understanding of the fluid migration mechanism.

In this report, we present the results of our two-week ocean bottom seismometer monitoring of an active seepage site in the Haima cold seep area, located in the northwestern South China Sea (Figure 1). Five SDEs have been identified from the continuous record by visual inspection followed by spectrum analysis, the first time that SDEs have been reported in the South China Sea. The nature of these SDEs and their implication for methane seepage are then interpreted by integrating the SDE data with previous seismic and multi-beam survey results.

2. Geological Background and Previous Work

The monitored seepage site is located at the Haima cold seep in the Qiongdongnan Sea area, on the northwestern slope of the South China Sea. The Haima cold seep was first discovered in 2015 in data from the "Haima" Remotely Operative Vehicle (ROV; Liang QY et al., 2017); in 2016, four acoustic flares were observed in multi-beam water column data collected in the same area (Liu B and Liu SX, 2017). Based on these acoustic flares, four seepage sites have been identified (Liu B et al., 2021a). The cold seep site linked to plume D is the site we monitored with an OBS device and is the study area of this work (Figure 1).

The Haima cold seep area has been extensively studied using a variety of techniques, including geophysical, geo-chemical, and drilling techniques. Seismic profiles depict the pipe structures beneath the active seepage sites (Yang L et al., 2018; Liu B et al., 2021a). These pipe structures act as fluid migration pathways; some of them extend from the seafloor to below the Bottom-Simulating Reflector (BSR). There are many gas pockets within the pipe structure and near to the seafloor, according to seismic diffraction research (Liu B et al., 2021b). Moreover, a large blanking zone exists beneath the studied site from the sub-bottom profile (Figure 1d); this has been interpreted as a free gas zone (Liu B and Liu SX, 2017).

Abundant gas hydrates are spread through this region. During the gas hydrate drilling program GMGS5, samples of deeply buried gas hydrates were obtained. At numerous locations, near-seafloor gas hydrates have been discovered 4–8 meters below the seafloor (Yang L et al., 2018). Our knowledge of fluid movement patterns and seepage activities in this regions is constrained by geo-chemical analyses (Guan H et al., 2018; Wang J et al., 2018; Hu Y et al., 2019)

Despite several comprehensive assessments of the Haima cold seep, the current seepage intensity is not well understood, due to lack of continuous monitoring. Acoustic flares indicate that certain sites still experience active seepage. However, the common presence of dead bivalves suggests a decline in seepage activity over time (Liang QY et al., 2017).

3. Data and Methods

3.1 Data Acquisition

To study potential micro-events produced by fluid migration, we deployed a Geopro-type four-component ocean bottom seismometer at plume D site to monitor the seepage process.

The OBS was equipped with three orthogonal geophones (*X*, *Y* and *Z* components, with a corner frequency of 2 Hz); attached to the OBS frame was a hydrophone (*H* component). The four detectors are also called four channels. The OBS was deployed on 6 November 2021 using the "Haima" ROV at a water depth of 1441 m. It was recovered on 19 November 2021. The instrument recorded data continuously at a sampling rate of 4 ms. This corresponds to the Nyquist frequency of 125 Hz. The data cover the launch of the OBS, the duration of the deployment, and the recovery of the OBS. The raw data, retrieved from the instrument, were converted to the SAC format.

3.2 Event Identification and Analysis

We primarily use Matlab for data analysis. The data were initially transformed into two-day-long mat-format files. To assess the general quality of the data and get a rough idea of the events that may have been detected, we scanned all of the data files. The data spanning 5/11 to 8/11 are displayed in Figures 2 and 3; data from 9/11 to 18/11 are displayed in the Supplementary Materials. Data in Figure 2 are from before the OBS was deployed on the seafloor. Figure 3 presents data recorded after OBS deployment. It can be observed that in general, the hydrophone — see Figures 2a and 3a — records many more events than the geophone channels. This is partially because many events occur in the water column that are unrelated to seafloor activity, such as shipping, current-

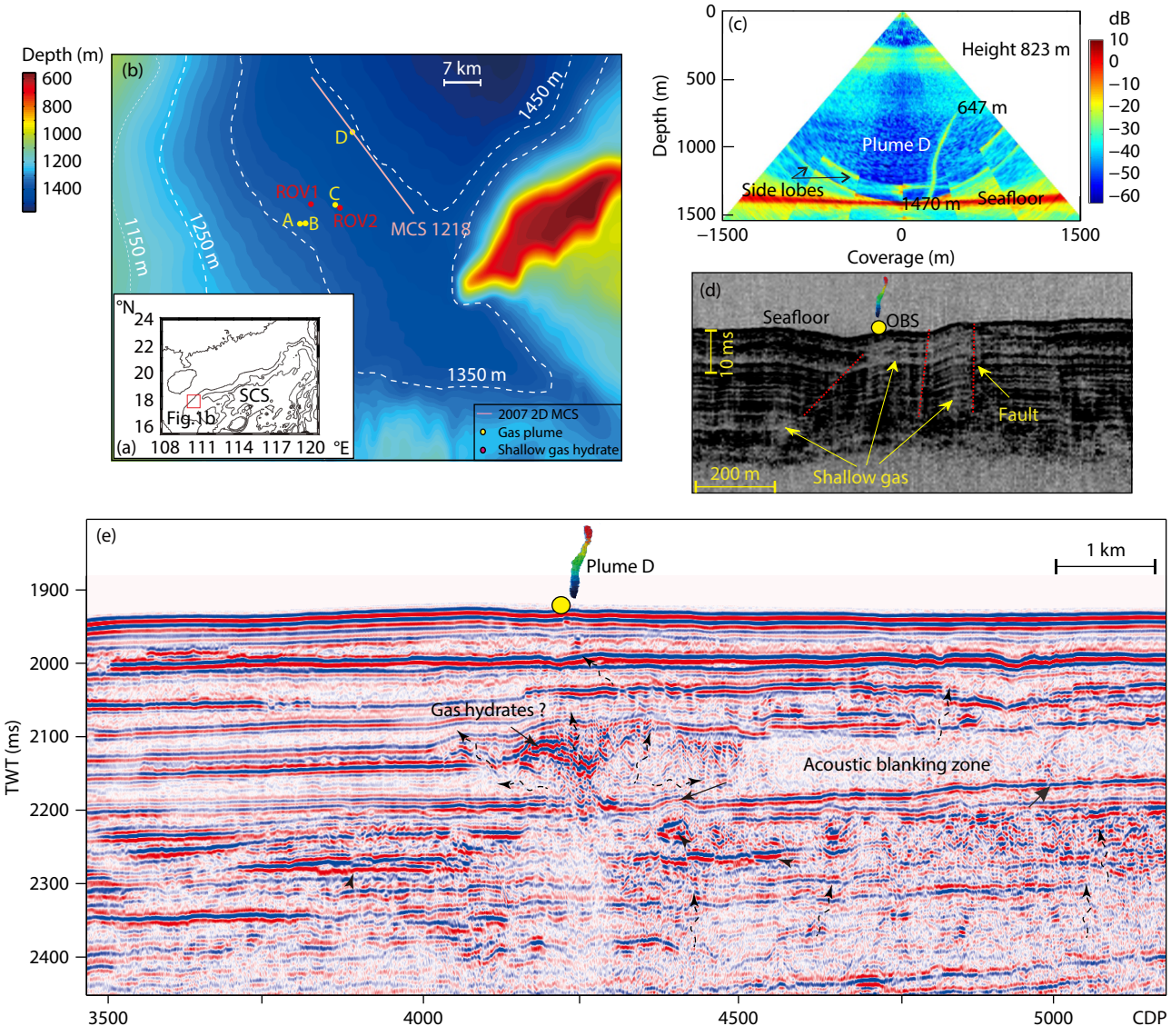

Figure 1. The area monitored by our ocean bottom seismometer. (a) Background setting of the monitored site. (b) Multi-beam bathymetric map of the area around the site. (c) Gas bubbles plume in the multi-beam water-column data (Liu B and Liu SX, 2017). (d) Sub-bottom profiler data passing through the site. The profile was acquired in 2013 using Parasound P70. The frequency range is 1000–3000 Hz (Liu B and Liu SX, 2017). (e) 2D multi-channel seismic profile that crosses plume D.

induced events, and activity of marine mammals; hydrophones are more sensitive to these water-column events than are geophones.

In this work, we manually identify and pick events of interest by visual inspection. As mentioned above, we deployed the OBS for the purpose of studying potential micro-events produced by fluid migration; therefore, short duration events are our top priority. But other types of signal were also picked and were chosen for analysis. Once picked, an event was subjected to spectrum analysis in order to delineate more information. Spectrum analysis can distinguish signals at different frequency bands, which can help determine teach signal's nature.

4. Results

Four distinct categories of event caught our attention: ROV-related signals, nearby shipping noise, a natural earthquake, and SDEs.

4.1 ROV-related Signals

The red box in Figure 2 indicates the signals linked to operation of the ROV, which were identified by correlating them with times when the ROV was active. These ROV-related signals are quite strong, especially as recorded by the hydrophone (a). Although all four channels were sensitive to these signals, they exhibit different characteristics. As shown in Figure 4, three stages of the ROV's mission can be seen in these data: (1) ROV sailing, (2) ROV launching the OBS, (3) ROV leaving. Very large and long time-lasting signals were produced when the ROV sailed underwater, as indicated by the black box in Figure 4. The signal is an order of magnitude weaker when the machinery hand launches the OBS (yellow box). The OBS is positioned on the ocean floor at 14:23; the ROV then

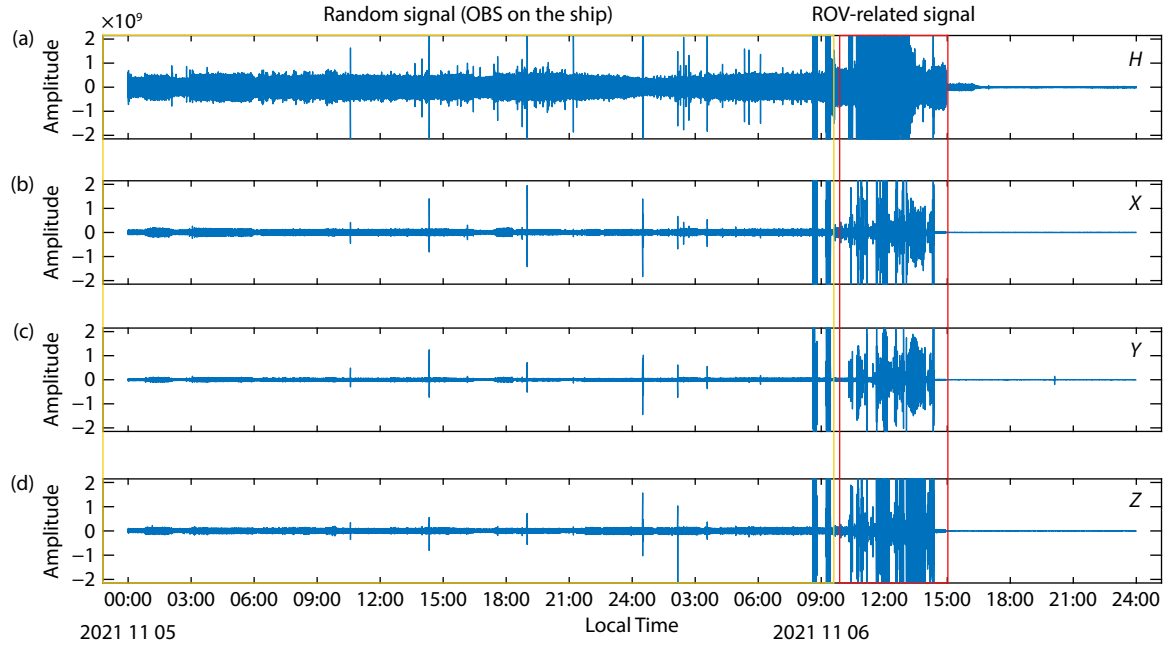

Figure 2. Data collected prior to the deployment of OBS on the ocean floor. (a) is data from the hydrophone; (b–d) are the *X*, *Y*, and *Z* components of the seismographic record from the geophones. The yellow box indicates signals recorded when the OBS was on the ship and the ship was sailing. Most are random signals. The red box indicates signals linked to operation of the "Haima" ROV (remotely operated vehicle).

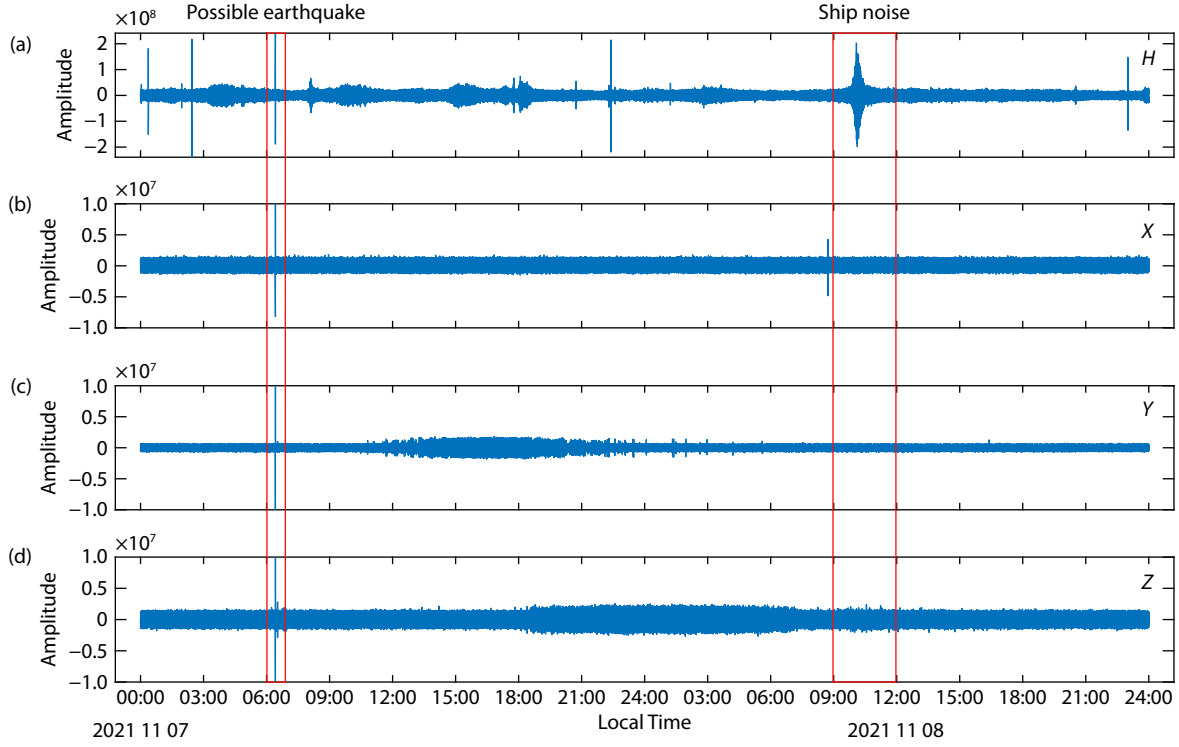

Figure 3. Data collected after the OBS was deployed on the ocean floor. (a) is data from the hydrophone; (b–d) are the *X*, *Y*, and *Z* components ofthe seismographic record from the geophones. Compared to signals associated with ship sailing and ROV operation (Figure 2), these data are anorder of magnitude weaker.

leaves the OBS. The recorded signal becomes weaker when the ROV departs the OBS (red box). Since the ROV-related disturbance at this stage occurs in the water column, only the hydrophone channel records significant signal (Figure 4a).

4.2 Shipping Noise

Undersea noise generated by ships is very common. The propeller is the dominant source of noise from nearby passing ships; it is easily identified on both the waveform and the time-frequency

spectrograms (McKenna et al., 2013; Niu HQ et al., 2017). Figure 5 shows an example of ship noise and its spectrogram. The ship noise lasts for nearly half an hour over a broad-band component (20–100 Hz). Only the hydrophone (Figures 5d and 5c) records

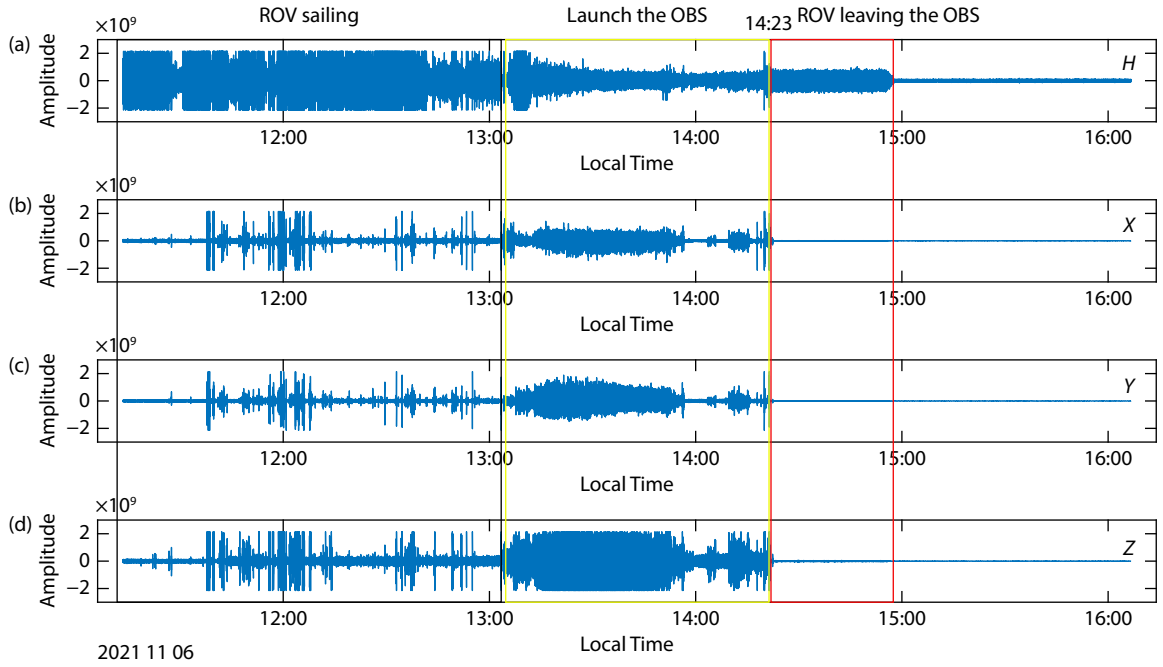

Figure 4. Events linked with ROV operation. (a) is data from the hydrophone; (b)–(d) are the *X*, *Y*, and *Z* components of the seismographic record from the geophones.

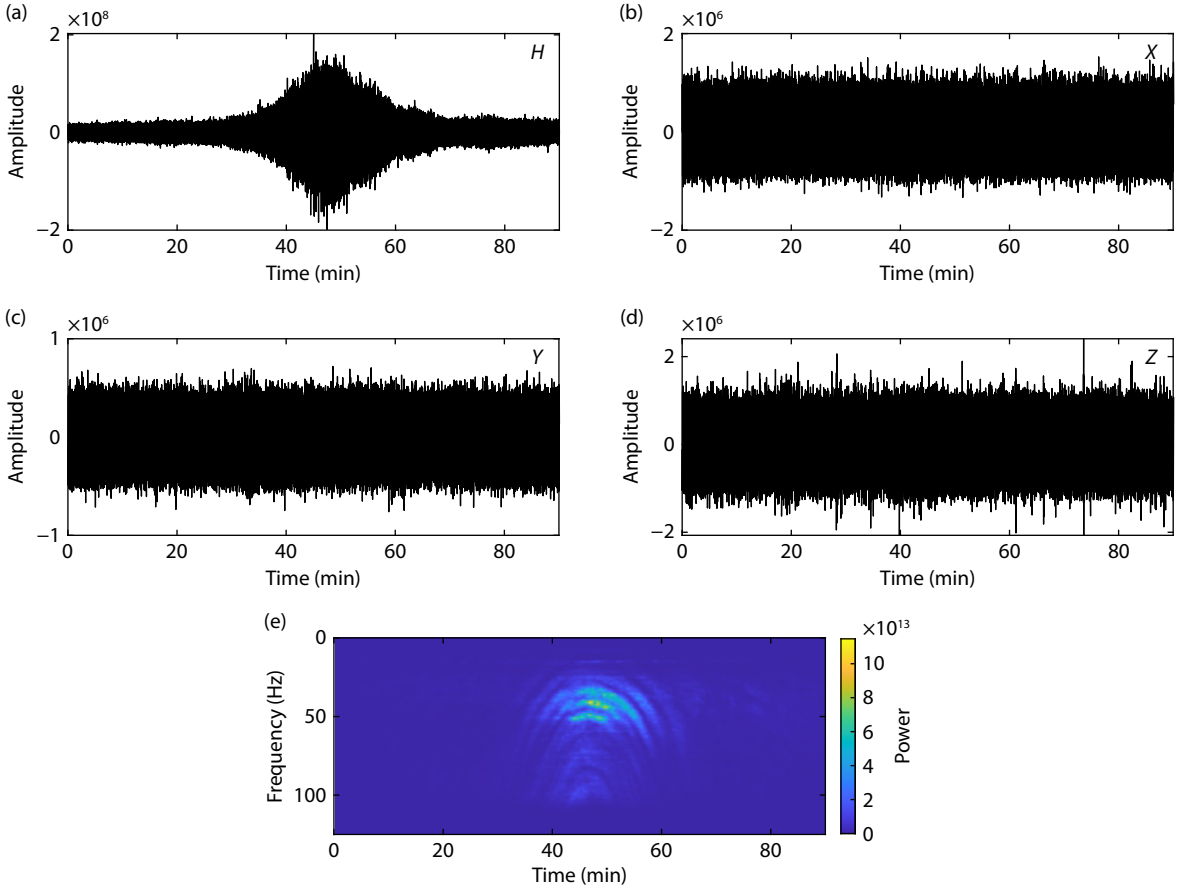

Figure 5. An example of shipping noise. (a–d) show the waveforms of the shipping noise on the geophones and the hydrophone. (e) is the spectrogram of (a). The spectrogram was computed with the matlab function *pspectrum*.

ship noise; the other three channels, the geophones, do not. They record only background noise, as can be seen from Figures 5a–c.

4.3 Local Earthquake

Land seismometers are often too far away to reliably detect an earthquake that occurs in the remote ocean. A hydrophone can occasionally record an earthquake, though, because when an earthquake hits the ocean bottom, an acoustic wave may be set off at the water-sediment contact. An ocean bottom seismometer, however, can reliably capture local earthquakes. By visual inspection, we identified a possible local earthquake in data from our OBS (Figure 6). It lasts for about 6 seconds. It was recorded on all four channels of the OBS — the three geophones and the attached hydrophone. However, data on the different channels exhibit differences in frequency content.

4.4 SDEs

When an OBS is used to monitor the sub-seafloor fluid process, it frequently records signals that are distinct from local earthquakes in that they are characterized by a short duration (usually < 1 s) and a single pulse with no P and S phase. Only very strong SDEs can be captured on all channels, as numerous earlier studies have shown (Domel et al. 2022), hence we focus our search on the vertical channel (*Z*-component) of the OBS. Once a possible SDE was identified in the *Z*-channel, the waveforms on the other three channel were checked. Figure 7 shows an example of an SDE. (a)–(d) show the waveform of the SDE on each channel. The duration time is less than 1 s. This SDE was recorded by all the four channels; as expected, a larger amplitude appeared on the vertical channel. To better delineate a probable SDE, we next apply spectrum analysis. As reported in previous studies, SDEs are characterized by a relatively high frequencies (4–30 Hz). Therefore, spectrum analysis helps us further confirm the data as characteristic of an SDE.

Figures 7e–h show the spectral contents of Figures 7a–d. We observe a large difference between the spectrum content of the hydrophone data (Figure 7e) and data from the three geophone components (Figures 7f–h). The *X*, *Y* and *Z* components peak at

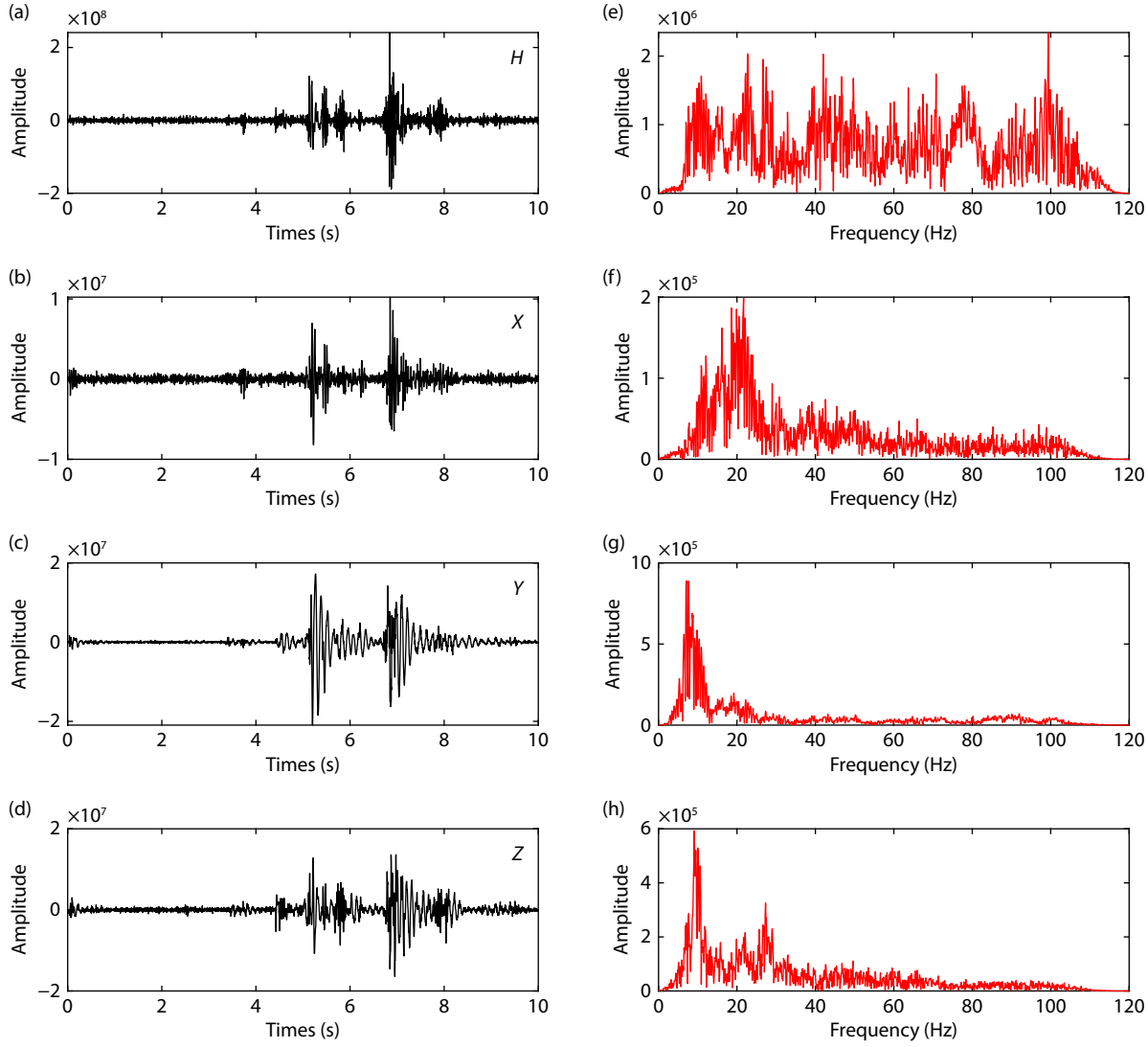

Figure 6. A possible local earthquake. (a) and (e) show the hydrophone data and its spectrum. (b) and (f) show the *X* component data and its spectrum. (c) and (g) show the *Y* component data and its spectrum. (d) and (h) show the *Z* component data and its spectrum.

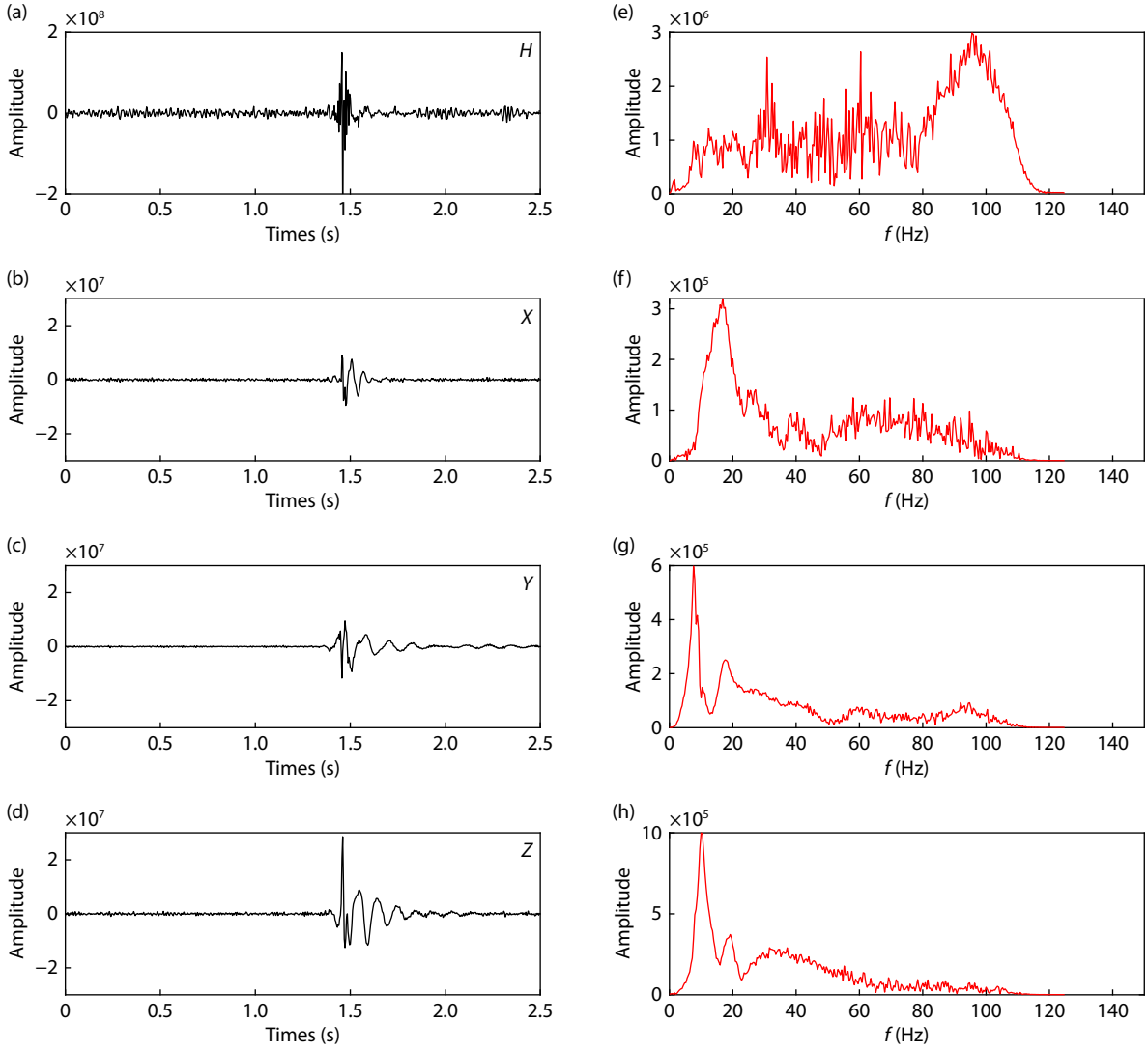

Figure 7. An example of a short duration event (SDE) recorded on all the four channels. (a) and (e) show the hydrophone data and its spectrum. (b) and (f) show the *X* component data and its spectrum. (c) and (g) show the *Y* component data and its spectrum. (d) and (h) show the *Z* component data and its spectrum.

10–20 Hz, while the hydrophone component has very strong energy over 100 Hz. One possible explanation is that hydrophone data are contaminated by much more high frequency background noise. High frequency background noise on the hydrophone can also be identified in its amplitude waveform (Figure 7a).

In the entire dataset, we identified five SDEs through visual inspection. Their waveforms, captured on the vertical channel, are shown in Figure 8, along with their frequency spectrums, derived using FFT. All five SDEs lasted for roughly 1 s. They exhibit a regular amplitude reduction in the coda and no secondary arrivals. With the exception of SDE 5, which includes an additional peak at 7 Hz, these signals all peak at 10 Hz. These characteristics of waveform and spectrum have already been reported in many other settings, for example, in drilling operations (Ugalde et al., 2019), at the Galicia Margin (Díaz et al., 2007), in the Sea of Marmara (Tary et al., 2012; Tsang-Hin-Sun et al., 2019), in the western Ionian Sea (Sgroi et al., 2021) and in the western Svalbard shelf (Franek et al., 2017).

Though different kinds of signals have been identified in past studies, in this work we are mainly focused on the SDEs. Other types of signals will not be further discussed in this report.

5. Discussion

5.1 The Nature of Short Duration Events

Though SDEs have been reported in many sea areas, their origin remains unclear. Several causal mechanisms have been proposed: (1) biological entities striking the instruments (Buskirk et al., 1981), (2) resonances from fluid-filled cracks (Díaz et al., 2007); (3) hydraulic fracturing (Bowman and Wilcock et al., 2014) and (4) fluid migration (Tary et al., 2012; Franek et al., 2017; Domel et al., 2022). In cold seep areas, gas migration is the most widely accepted source of SDEs. This interpretation has been supported by long-term monitoring experiments and very detailed analysis. For example, in the Western Svalbard shelf, an OBS was deployed to record data over a continuous 297-day period. After ruling out other sources as unlikely, the possibilities were narrowed down to gas seepage and sub-seafloor fluid migration (Franek et al., 2017).

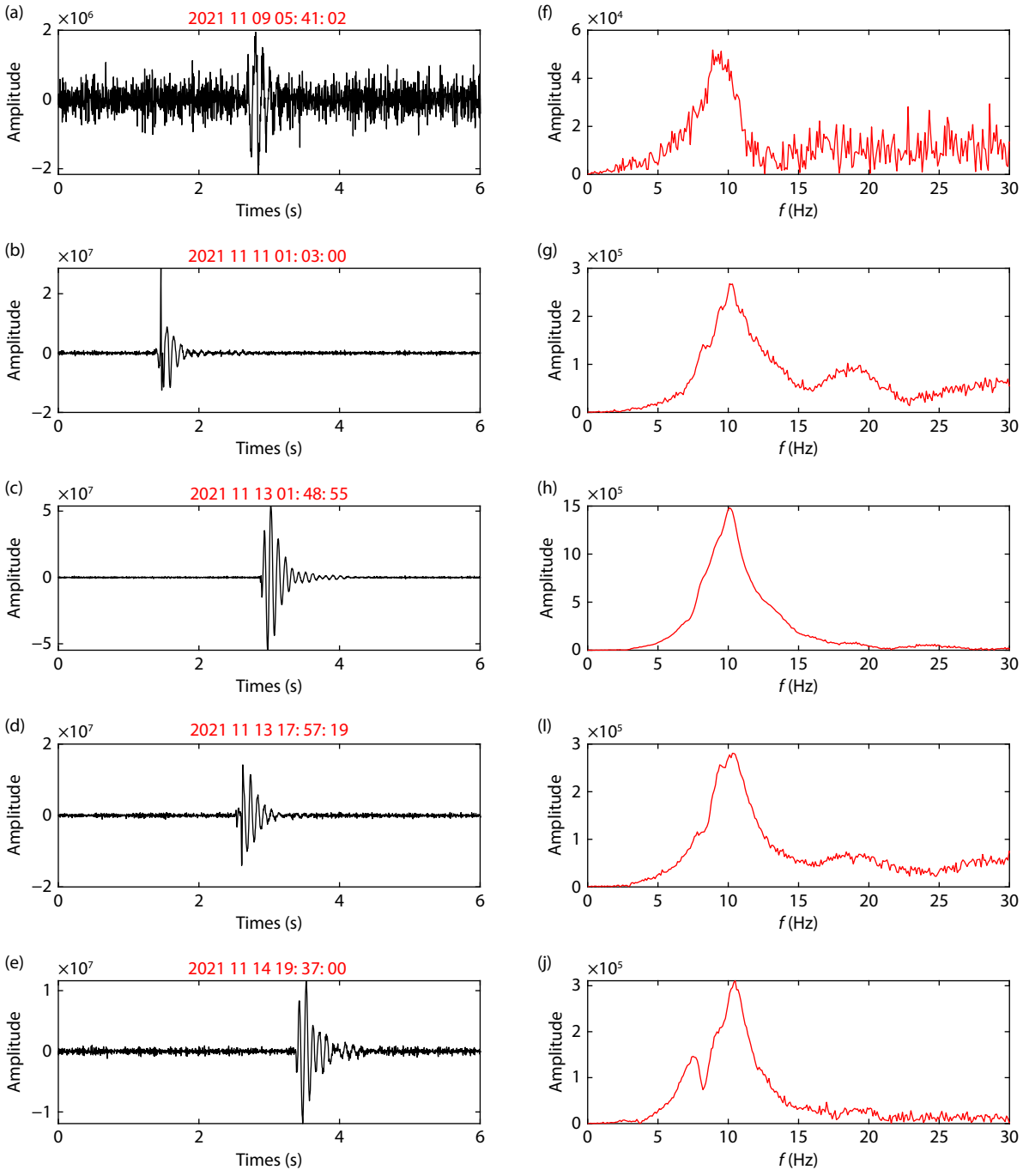

Figure 8. All five SDEs observed in the two-week observation period. (a–e) show the hydrophone waveform data of the five SDEs and (f–j) show their corresponding spectrums.

This interpretation is also supported by laboratory experiments (Batsi et al., 2019) and numerical-modeling experiments (Tary et al., 2012).

Our observations are being conducted at the well-known Haima cold seep area. Specifically, the OBS is deployed at a gas seepage site (plume D) where a gas bubble plume was observed in 2016 (Liu B and Liu SX, 2017). As shown in the sub-bottom profile (Figure 1d), beneath the OBS site is an acoustic blanking zone approximately 200 m wide. This acoustic blanking zone in the sub-bottom profile indicates the presence of free gas in the shallow sub-seafloor beneath the OBS site. In addition, several faults can be traced from below the free gas zone to the seafloor. Therefore, our monitored site is similar to other environments where SDEs have previously been reported, and interpreted to be caused by fluid migration.

Within our 14-day-long dataset, we have identified five SDEs. As was already indicated, these SDEs resemble, both in terms of waveform and spectral features, SDEs that have been seen in other environments.

The above two facts lead us to attribute the SDEs to a fluid migration process beneath plume D. However, our currently available

data are not sufficient to rule out other mechanisms.

5.2 Seepage Intensity of the Haima Cold Seep

Knowledge of how seepage can vary is very important for assessing the potential impact of a cold seep. The geo-chemical method is widely used to infer seepage variability. For instance, in the Haima cold seep area, a major episode of carbonate precipitation between 6.1 ka and 5.1 ka BP (Liang QY et al., 2017) is suggested by the carbon isotopic analysis. However, chemical analysis can provide only long-term and large-scale information about seepage, and very little detail, if any, about how it has varied and may vary in the future. Moreover, the chemical method can tell little about the current stage. Both limitations make chemical analysis insufficient. Time-lapse geophysical surveys can provide short-term and small-scale information, and are thus sometimes used to infer seepage variability. For instance, 4D time-lapse seismic surveys are conducted at the Bullseye vent, northern Cascadia margin, to monitor the seepage process there, and have identified a change of seepage channel (Riedel, 2007); in the Gulf of Mexico, repeat observations suggest order-of-magnitude gas flow variability over times as short as hours (Jerram et al., 2015); however, time-lapse geophysical surveys are very expensive.

Recently, ocean bottom seismometers have been deployed to monitor the cold seep process by continuously recording events associated with known fluid migration. The seepage activity and its mechanism(s) may be inferred by analyzing such data records. For instance, in the Sea of Marmara, the high daily rate of SDE observations in the whole experiment suggests a highly active seepage (Tsang-Hin-Sun et al., 2019).

In our work, the SDEs we observed have been attributed to fluid migration beneath the plume D. Therefore, it can be inferred that fluid migration is still active at this monitored site. However, only five SDEs were observed during the 14-day long observation period — an occurrence rate that is much lower than observed in other cold seep areas. For example, the daily number of SDEs exceeds 100 in most of the monitoring time in the Sea of Marmar (Tsang-Hin-Sun et al., 2019). In the Western Svalbard shelf, over 220,000 SDEs were detected during over a 297-day period, yielding a mean rate of 32 events per hour (Franek et al., 2017). This contrast leads one to surmise that fluid migration is not occurring very actively at the plume D monitored site. As fluid migration is a necessary condition for seepage process, the seepage activity therefore is expected to be limited.

A previous study reported that dead bivalves were frequently found in the Haima cold seep location, suggesting that seepage activity has been declining over time (Liang QY et al., 2017). Our SDE observations seems to support the decline in seepage activity. However, in this monitoring experiment, the observation period was relatively short (only 14 days) compared to the 297-day-long experiment in the Western Svalbard shelf (Franek et al., 2017) and the four-month-long experiment in the Sea of Marama (Tary et al., 2012). Furthermore, only one monitoring station was deployed. To better understand the seepage process of the Haima cold seep, a longer observation period with more stations is required.

6. Conclusions

One of the seepage sites in the Haima cold seep area was monitored with an ocean bottom seismometer for the short period of 14 days. Several different types of signals were identified by visual inspection of the data, including ROV-related signals, shipping noises, a local earthquake, and SDEs. Five SDEs were found. All five exhibit a distinct frequency peak of about 10 Hz and durations of less than 1 s. Due to the proximity of the OBS to a known cold seepage location and the fact that these SDEs resemble the SDEs recorded in other cold seep situations with different types of OBSs, we link these SDEs to the fluid migration process. Our detection of SDEs indicates an on-going fluid migration beneath the site. But the low SDE occurrence rate that we observed may indicate that the fluid migration process in this location is not very active, which is consistent with a decline in the seepage activity previously observed from chemical analysis. Our results represent the first discovery of micro-events linked to the cold seep process in the South China Sea and provide additional constraints on the activity of the cold seep process.

Data and code availability

The experimental data are not publicly available but can be requested by contacting the corresponding author.

Conflicts of Interest

The authors declare no conflicts of interest regarding the publication of this paper.

Acknowledgments

This study was financially supported by the Key Research and Development Project of Guangdong Province (Grant: 2020B1111510001). This investigation is further supported by the Project of Sanya Yazhou Bay Science and Technology City (Grant No：SCKJ-JYRC-2022-14) and the National Natural Science Foundation of China (Grant No: 92262304). A great thanks is offered to the crew members and scientists who participated in the acquisition of the multi-beam data in 2016, the sub-bottom profile in 2013, the seismic data in 2007, and the OBS monitoring data in 2021. We thank Guangzhou Marine Geological Survey for permission to publish the results.

References

Attias, E., Weitemeyer, K., Minshull, T. A., Best, A. I., Sinha, M., Jegen-Kulcsar, M., Hölz, S., and Berndt, C. (2016). Controlled-source electromagnetic and seismic delineation of subseafloor fluid flow structures in a gas hydrate province, offshore Norway. *Geophys. J. Int.*, *206*(2), 1093–1110. https://doi.org/10.1093/gji/ggw188

Bangs, N. L. B., Hornbach, M. J., and Berndt, C. (2011). The mechanics of intermittent methane venting at South Hydrate Ridge inferred from 4D seismic surveying. *Earth Planet. Sci. Lett.*, *310*(1-2), 105–112. https://doi.org/10.1016/j.epsl.2011.06.022

Batsi, E., Tsang-Hin-Sun, E., Klingelhoefer, F., Bayrakci, G., Chang, E. T. Y., Lin, J. Y., Dellong, D., Monteil, C., and Géli, L. (2019). Nonseismic signals in the ocean: Indicators of deep sea and seafloor processes on ocean-bottom seismometer data. *Geochem. Geophys. Geosyst.*, *20*(8), 3882–3900. https://doi.org/10.1029/2019GC008349

Bayon, G., Henderson, G. M., Etoubleau, J., Caprais, J. C., Ruffine, L., Marsset, T., Dennielou, B., Cauquil, E., Voisset, M., and Sultan, N. (2015). U-Th isotope constraints on gas hydrate and pockmark dynamics at the Niger delta margin. *Marine Geology*, *370*, 87–98. https://doi.org/10.1016/j.margeo.2015.10.012

Bowman, D. C., and Wilcock, W. S. D. (2014). Unusual signals recorded by ocean bottom seismometers in the flooded caldera of Deception Island volcano: Volcanic gases or biological activity. *Antarct. Sci.*, *26*(3), 267–275. https://doi.org/10.1017/S0954102013000758

Brothers, D. S., Ruppel, C., Kluesner, J. W., Ten Brink, U. S., Chaytor, J. D., Hill, J. C., Andrews, B. D., and Flores, C. (2014). Seabed fluid expulsion along the upper slope and outer shelf of the U.S. Atlantic continental margin. *Geophys. Res. Lett.*, *41*(1), 96–101. https://doi.org/10.1002/2013GL058048

Buskirk, R. E., Frohlich, C., Latham, G. V., Chen, A. T., and Lawton, J. (1981). Evidence that biological activity affects Ocean Bottom Seismograph recordings. *Mar. Geophys. Res.*, *5*(2), 189–205. https://doi.org/10.1007/BF00163479

Chen, F., Hu, Y., Feng, D., Zhang, X., Cheng, S. H., Cao, J., Lu, H. F., and Chen, D. F. (2016). Evidence of intense methane seepages from molybdenum enrichments in gas hydrate-bearing sediments of the northern South China Sea. *Chem. Geol.*, *443*, 173–181. https://doi.org/10.1016/j.chemgeo.2016.09.029

Crémière, A., Lepland, A., Chand, S., Sahy, D., Kirsimäe, K., Bau, M., Whitehouse, M. J., Noble, S. R., Martma, T., … Brunstad, H. (2016). Fluid source and methane-related diagenetic processes recorded in cold seep carbonates from the Alvheim channel, central North Sea. *Chem. Geol.*, *432*, 16–33. https://doi.org/10.1016/j.chemgeo.2016.03.019

Crutchley, G. J., Pecher, I. A., Gorman, A. R., Henrys, S. A., and Greinert, J. (2010). Seismic imaging of gas conduits beneath seafloor seep sites in a shallow marine gas hydrate province, Hikurangi Margin, New Zealand. *Mar. Geol.*, *272*(1-4), 114–126. https://doi.org/10.1016/j.margeo.2009.03.007

Díaz, J., Gallart, J., and Gaspà, O. (2007). Atypical seismic signals at the Galicia Margin, North Atlantic Ocean, related to the resonance of subsurface fluid-filled cracks. *Tectonophysics*, *433*(1-4), 1–13. https://doi.org/10.1016/j.tecto.2007.01.004

Domel, P., Singhroha, S., Plaza-Faverola, A., Schlindwein, V., Ramachandran, H., and Bünz, S. (2022). Origin and periodic behavior of short duration signals recorded by seismometers at Vestnesa Ridge, an active seepage site on the West-Svalbard continental margin. *Front. Earth Sci.*, *10*, 831526. https://doi.org/10.3389/feart.2022.831526

Feng, D., and Chen, D. F. (2015). Authigenic carbonates from an active cold seep of the northern South China Sea: New insights into fluid sources and past seepage activity. *Deep Sea Res. Part II: Top. Stud. Oceanogr.*, *122*, 74–83. https://doi.org/10.1016/j.dsr2.2015.02.003

Franchi, F., Rovere, M., Gamberi, F., Rashed, H., Vaselli, O., and Tassi, F. (2017). Authigenic minerals from the Paola Ridge (southern Tyrrhenian Sea): Evidences of episodic methane seepage. *Mar. Petrol. Geol.*, *86*, 228–247. https://doi.org/10.1016/j.marpetgeo.2017.05.031

Franek, P., Plaza-Faverola, A., Mienert, J., Buenz, S., Ferré, B., and Hubbard, A. (2017). Microseismicity linked to gas migration and leakage on the western Svalbard shelf. *Geochem. Geophys. Geosyst.*, *18*(12), 4623–4645. https://doi.org/10.1002/2017GC007107

Goswami, B. K., Weitemeyer, K. A., Minshull, T. A., Sinha, M. C., Westbrook, G. K., Chabert, A., Henstock, T. J., and Ker, S. (2015). A joint electromagnetic and seismic study of an active pockmark within the hydrate stability field at the Vestnesa Ridge, West Svalbard margin. *J. Geophys. Res.: Solid Earth*, *120*(10), 6797–6822. https://doi.org/10.1002/2015JB012344

Goswami, B. K., Weitemeyer, K. A., Minshull, T. A., Sinha, M. C., Westbrook, G. K., and Marín-Moreno, H. (2016). Resistivity image beneath an area of active methane seeps in the west Svalbard continental slope. *Geophys. J. Int.*, *207*(2), 1286–1302. https://doi.org/10.1093/gji/ggw330

Greinert, J., Artemov, Y., Egorov, V., De Batist, M., and McGinnis, D. (2006). 1300-m-high rising bubbles from mud volcanoes at 2080 m in the Black Sea: Hydroacoustic characteristics and temporal variability. *Earth Planet. Sci. Lett.*, *244*(1-2), 1–15. https://doi.org/10.1016/j.epsl.2006.02.011

Guan, H., Birgel, D., Peckmann, J., Liang, Q., Feng, D., Yang, S., Liang, J., Tao, J., Wu, N., Chen, D. (2018). Lipid biomarker patterns of authigenic carbonates reveal fluid composition and seepage intensity at Haima cold seeps, South China Sea. *Journal of Asian Earth Sciences*, *168*, 163–172. https://doi.org/10.1016/j.jseaes.2018.04.035

He, T., Spence, G. D., Wood, W. T., Riedel, M., and Hyndman, R. D. (2009). Imaging a hydrate-related cold vent offshore Vancouver Island from deep-towed multichannel seismic data. *Geophysics*, *74*(2), B23–B36. https://doi.org/10.1190/1.3072620

Hsu, H. H., Liu, C. S., Morita, S., Tu, S. L., Lin, S., Machiyama, H., Azuma, W., Ku, C. Y., and Chen, S. C. (2018). Seismic imaging of the Formosa Ridge cold seep site offshore of southwestern Taiwan. *Mar. Geophys. Res.*, *39*(4), 523–535. https://doi.org/10.1007/s11001-017-9339-y

Hu, Y., Luo, M., Liang, Q., Chen, L., Feng, D., Yang, S., Liang, J., Chen, D. (2019). Pore fluid compositions and inferred fluid flow patterns at the Haima cold seeps of the South China Sea. *Marine and Petroleum Geology*, *103*, 29–40. https://doi.org/10.1016/j.marpetgeo.2019.01.007

Jerram, K., Weber, T. C., and Beaudoin, J. (2015). Split-beam echo sounder observations of natural methane seep variability in the northern Gulf of Mexico. *Geochem. Geophys. Geosyst.*, *16*(3), 736–750. https://doi.org/10.1002/2014GC005429

Judd, A. G., Hovland, M., Dimitrov, L. I., García Gil, S., and Jukes, V. (2002). The geological methane budget at continental margins and its influence on climate change. *Geofluids*, *2*(2), 109–126. https://doi.org/10.1046/j.1468-8123.2002.00027.x

Judd, A. G. (2003). The global importance and context of methane escape from the seabed. *Geo-Mar. Lett.*, *23*(3-4), 147–154. https://doi.org/10.1007/s00367-003-0136-z

Li, N., Feng, D., Chen, L. Y., Wang, H. B., and Chen, D. F. (2016). Using sediment geochemistry to infer temporal variation of methane flux at a cold seep in the South China Sea. *Mar. Petrol. Geol.*, *77*, 835–845. https://doi.org/10.1016/j.marpetgeo.2016.07.026

Liang, Q. Y., Hu, Y., Feng, D., Peckmann, J., Chen, L. Y., Yang, S. X., Liang, J. Q., Tao, J., and Chen, D. F. (2017). Authigenic carbonates from newly discovered active cold seeps on the northwestern slope of the South China Sea: Constraints on fluid sources, formation environments, and seepage dynamics. *Deep Sea Res. Part I: Oceanogr. Res. Pap.*, *124*, 31–41. https://doi.org/10.1016/j.dsr.2017.04.015

Liu, B., and Liu, S. X. (2017). Gas bubble plumes observed at north slope of South China Sea from multi-beam water column data. *Haiyang Xuebao* (*in Chinese*), *39*(9), 83–89. https://doi.org/10.3969/j.issn.0253-4193.2017.09.008

Liu, B., Chen, J. X., Yang, L., Duan, M. L., Liu, S. X., Guan, Y. X., and Shu, P. C. (2021a). Multi-beam and seismic investigations of the active Haima cold seeps, northwestern South China Sea. *Acta Oceanol. Sin.*, *40*(7), 183–197. https://doi.org/10.1007/s13131-021-1721-6

Liu, B., Yang, L., Chen, J. X., Azevedo, L., and Han, T. G. (2021b). Seismic diffraction analysis of a fluid escape pipe beneath the submarine gas bubble plume in the Haima cold seep area. *Geofluids*, *2021*, 9945548. https://doi.org/10.1155/2021/9945548

Marín-Moreno, H., Minshull, T. A., Westbrook, G. K., Sinha, B., and Sarkar, S. (2013). The response of methane hydrate beneath the seabed offshore Svalbard to ocean warming during the next three centuries. *Geophys. Res. Lett.*, *40*(19), 5159–5163. https://doi.org/10.1002/grl.50985

McKenna, M. F., Wiggins, S. M., and Hildebrand, J. A. (2013). Relationship between container ship underwater noise levels and ship design, operational and oceanographic conditions. *Sci. Rep.*, *3*, 1760. https://doi.org/10.1038/srep01760

Myhre, C. L., Ferré, B., Platt, S. M., Silyakova, A., Hermansen, O., Allen, G., Pisso, I., Schmidbauer, N., Stohl, A., … Mienert, J. (2016). Extensive release of methane from Arctic seabed west of Svalbard during summer 2014 does not influence the atmosphere. *Geophys. Res. Lett.*, *43*(9), 4624–4631. https://doi.org/10.1002/2016GL068999

Niu, H. Q., Ozanich, E., and Gerstoft, P. (2017). Ship localization in Santa Barbara Channel using machine learning classifiers. *J. Acoust. Soc. Am.*, *142*(5), EL455–EL460. https://doi.org/10.1121/1.5010064

Riedel, M., Spence, G. D., Chapman, N. R., and Hyndman, R. D. (2002). Seismic investigations of a vent field associated with gas hydrates, offshore Vancouver Island. *J. Geophys. Res.: Solid Earth*, *107*(B9), 2200. https://doi.org/10.1029/2001jb000269

Riedel, M., Novosel, I., Spence, G. D., Hyndman, R. D., Chapman, R. N., Solem, R. C., and Lewis, T. (2006). Geophysical and geochemical signatures associated with gas hydrate-related venting in the northern Cascadia margin. *GSA Bull.*,

118(1-2), 23–38. https://doi.org/10.1130/B25720.1

Riedel, M. (2007). 4D seismic time-lapse monitoring of an active cold vent, northern Cascadia margin. *Mar. Geophys. Res.*, *28*(4), 355–371. https://doi.org/10.1007/s11001-007-9037-2

Römer, M., Torres, M., Kasten, S., Kuhn, G., Graham, A. G. C., Mau, S., Little, C. T. S., Linse, K., Pape, T., … Bohrmann, G. (2014). First evidence of widespread active methane seepage in the Southern Ocean, off the sub-Antarctic island of South Georgia. *Earth Planet. Sci. Lett.*, *403*, 166–177. https://doi.org/10.1016/j.epsl.2014.06.036

Sarkar, S., Berndt, C., Minshull, T. A., Westbrook, G. K., Klaeschen, D., Masson, D. G., Chabert, A., and Thatcher, K. E. (2012). Seismic evidence for shallow gas-escape features associated with a retreating gas hydrate zone offshore west Svalbard. *J. Geophys. Res.*: *Solid Earth*, *117*(B9), B09102. https://doi.org/10.1029/2011JB009126

Sgroi, T., Polonia, A., Beranzoli, L., Billi, A., Bosman, A., Costanza, A., Cuffaro, M., D'Anna, G., De Caro, M., … Doglioni, C. (2021). One year of seismicity recorded through ocean bottom seismometers illuminates active tectonic structures in the Ionian Sea (Central Mediterranean). *Front. Earth Sci.*, *9*, 661311. https://doi.org/10.3389/feart.2021.661311

Suess, E. (2014). Marine cold seeps and their manifestations: geological control, biogeochemical criteria and environmental conditions. *Int. J. Earth Sci.*, *103*(7), 1889–1916. https://doi.org/10.1007/s00531-014-1010-0

Tary, J. B., Géli, L., Guennou, C., Henry, P., Sultan, N., Çağatay, N., and Vidal, V. (2012). Microevents produced by gas migration and expulsion at the seabed: A study based on sea bottom recordings from the Sea of Marmara. *Geophys. J. Int.*, *190*(2), 993–1007. https://doi.org/10.1111/j.1365-246X.2012.05533.x

Tsang-Hin-Sun, E., Batsi, E., Klingelhoefer, F., and Géli, L. (2019). Spatial and temporal dynamics of gas-related processes in the Sea of Marmara monitored with ocean bottom seismometers. *Geophys. J. Int.*, *216*(3), 1989–2003. https://doi.org/10.1093/gji/ggy535

Ugalde, A., Gaite, B., Ruiz, M., Villaseñor, A., and Ranero, C. R. (2019). Seismicity and noise recorded by passive seismic monitoring of drilling operations offshore the eastern Canary Islands. *Seismol. Res. Lett.*, *90*(4), 1565–1576. https://doi.org/10.1785/0220180353

Wang, J., Wu, S., Kong, X., Ma, B., Li, W., Wang, D., Gao, J., Chen, W. (2018). Subsurface fluid flow at an active cold seep area in the Qiongdongnan Basin, northern South China Sea. *Journal of Asian Earth Sciences*, *168*, 48–56. https://doi.org/10.1016/j.jseaes.2018.06.001

Westbrook, G. K., Thatcher, K. E., Rohling, E. J., Piotrowski, A. M., Pälike, H., Osborne, A. H., Nisbet, E. G., Minshull, T. A., Lanoisellé, M., … Aquilina, A. (2009). Escape of methane gas from the seabed along the West Spitsbergen continental margin. *Geophys. Res. Lett.*, *36*(15), L15608. https://doi.org/10.1029/2009GL039191

Yang, L., Liu, B., Xu M. J., Liu, S. X., Guan, Y. X., and Gu, Y. (2018). Characteristics of active cold seepages in Qiongdongnan Sea Area of the northern South China Sea. *Chinese J. Geophys.* (*in Chinese*), *61*(7), 2905–2914. https://doi.org/10.6038/cjg2018L0374

Supplementary Materials for "Seismic monitoring of sub-seafloor fluid processes in the Haima cold seep area using an Ocean Bottom Seismometer (OBS)"

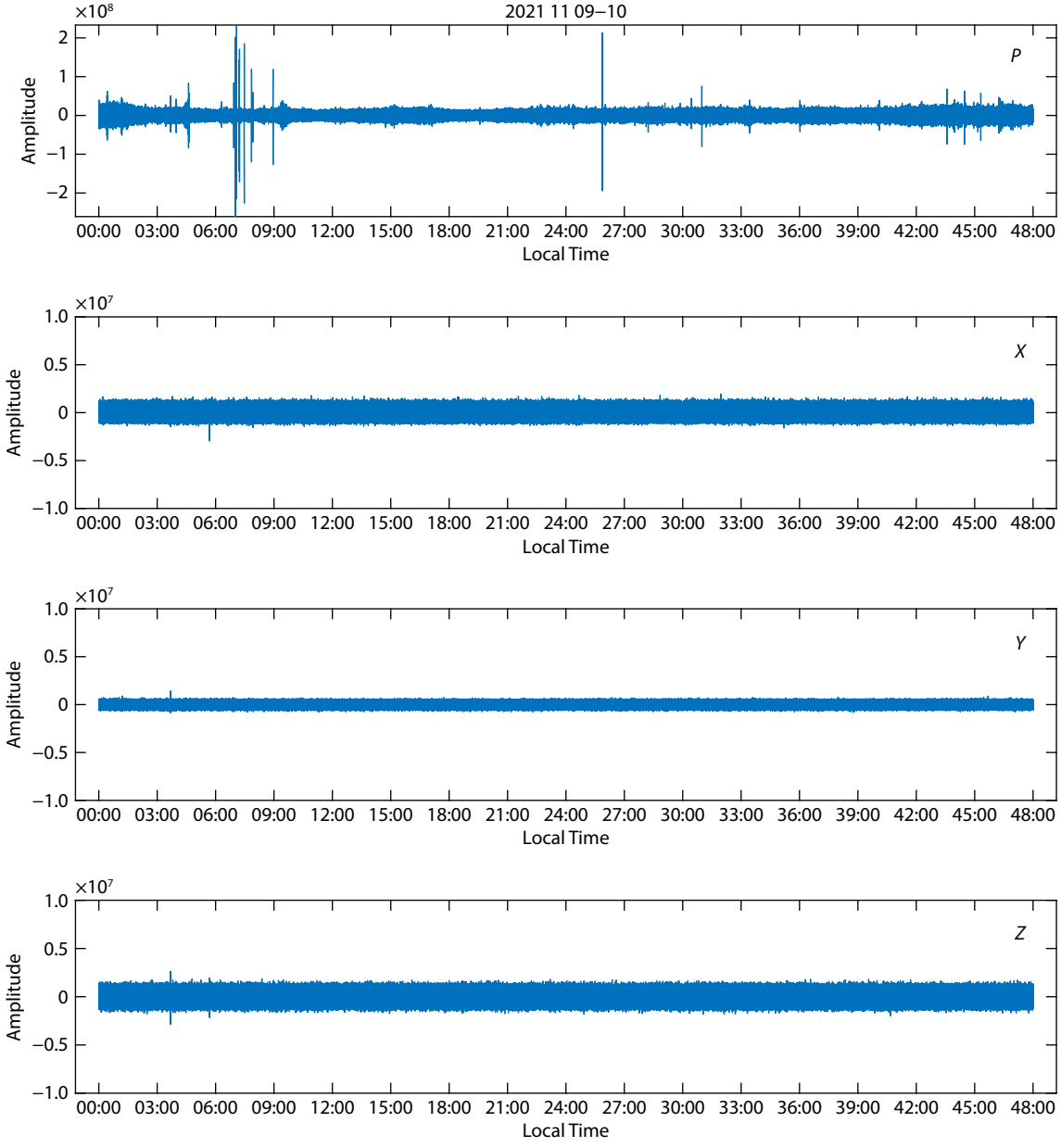

Figure S1. Four-component OBS data of 9/11–10/11. *H* is the data from hydrophone, and *X*, *Y*, *Z* are data from the three geophones.

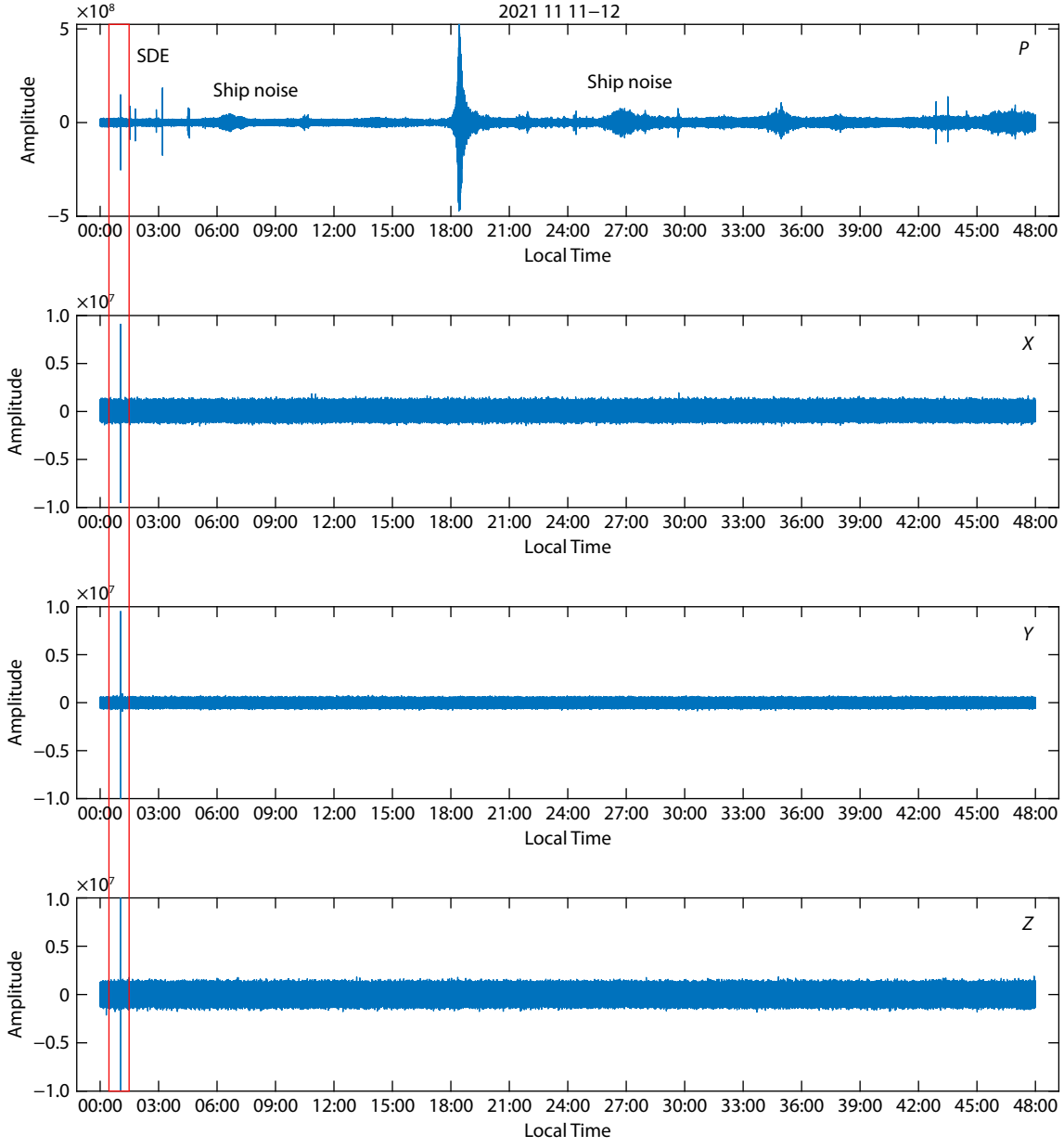

Figure S2. Four-component OBS data of 11/11–12/11. *H* is the data from hydrophone, and *X*, *Y*, *Z* are data from the three geophones.

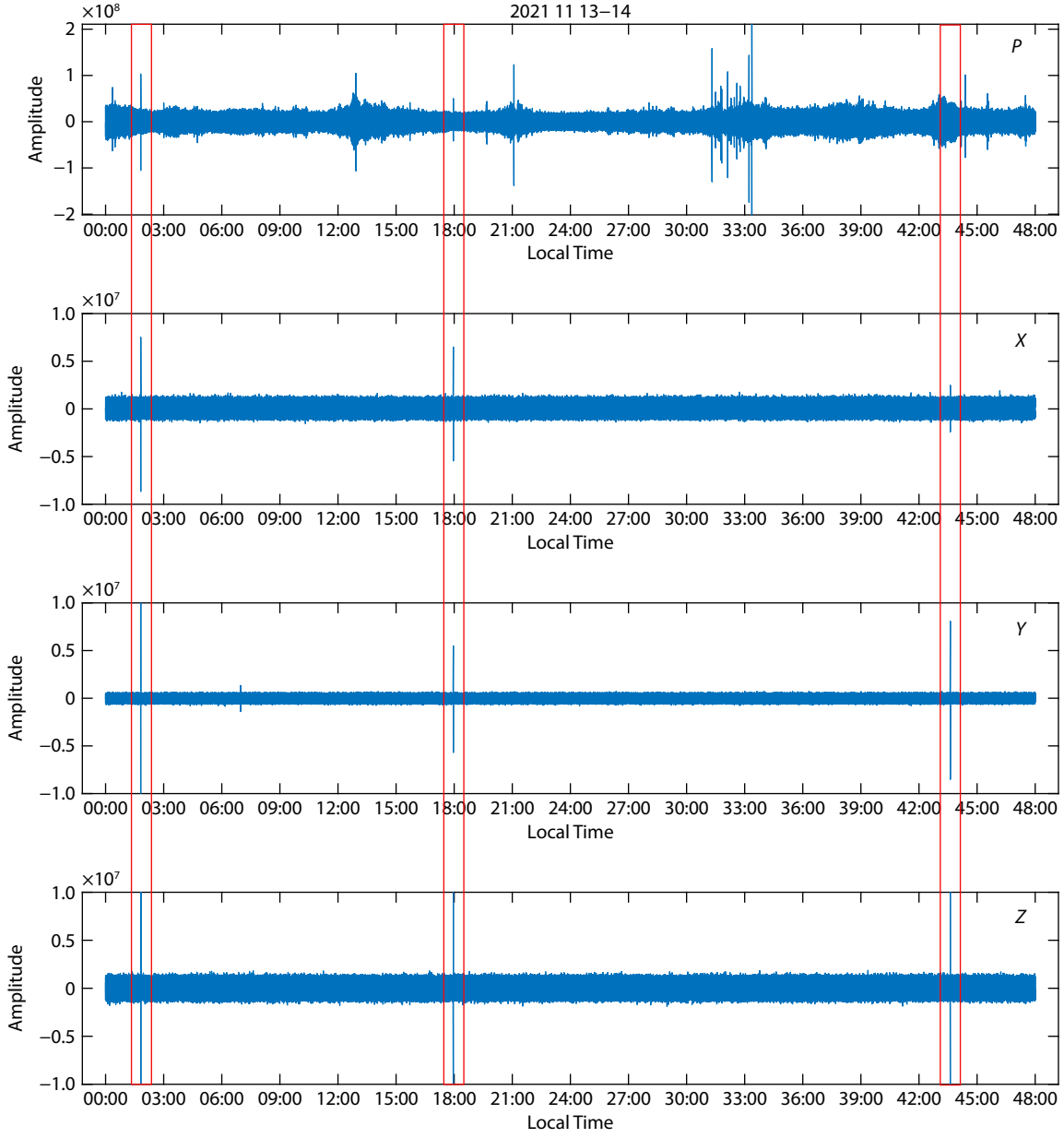

Figure S3. Four-component OBS data of 13/11–14/11. *H* is the data from hydrophone, and *X*, *Y*, *Z* are data from the three geophones.

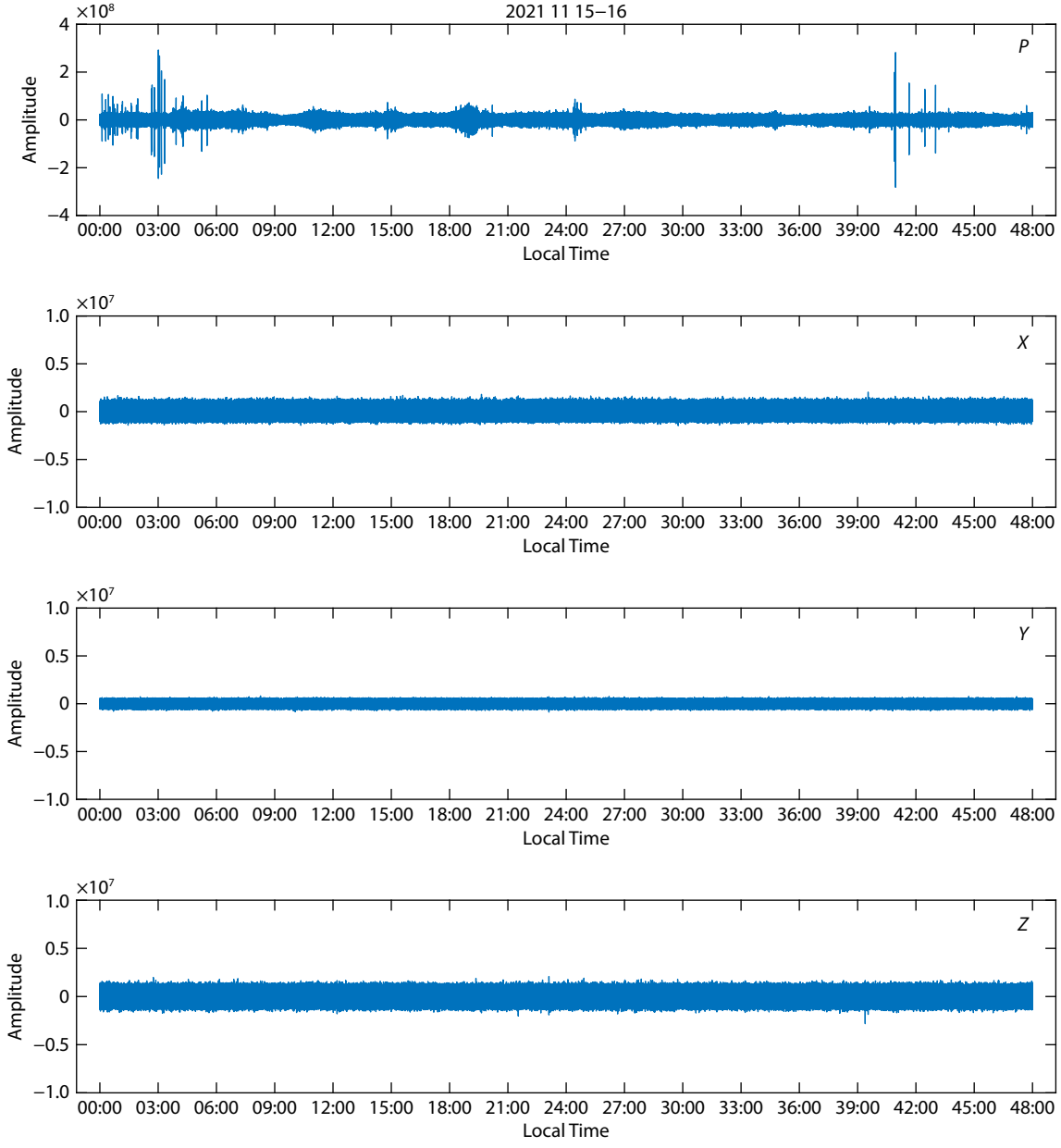

Figure S4. Four-component OBS data of 15/11–16/11. *H* is the data from hydrophone, and *X*, *Y*, *Z* are data from the three geophones.

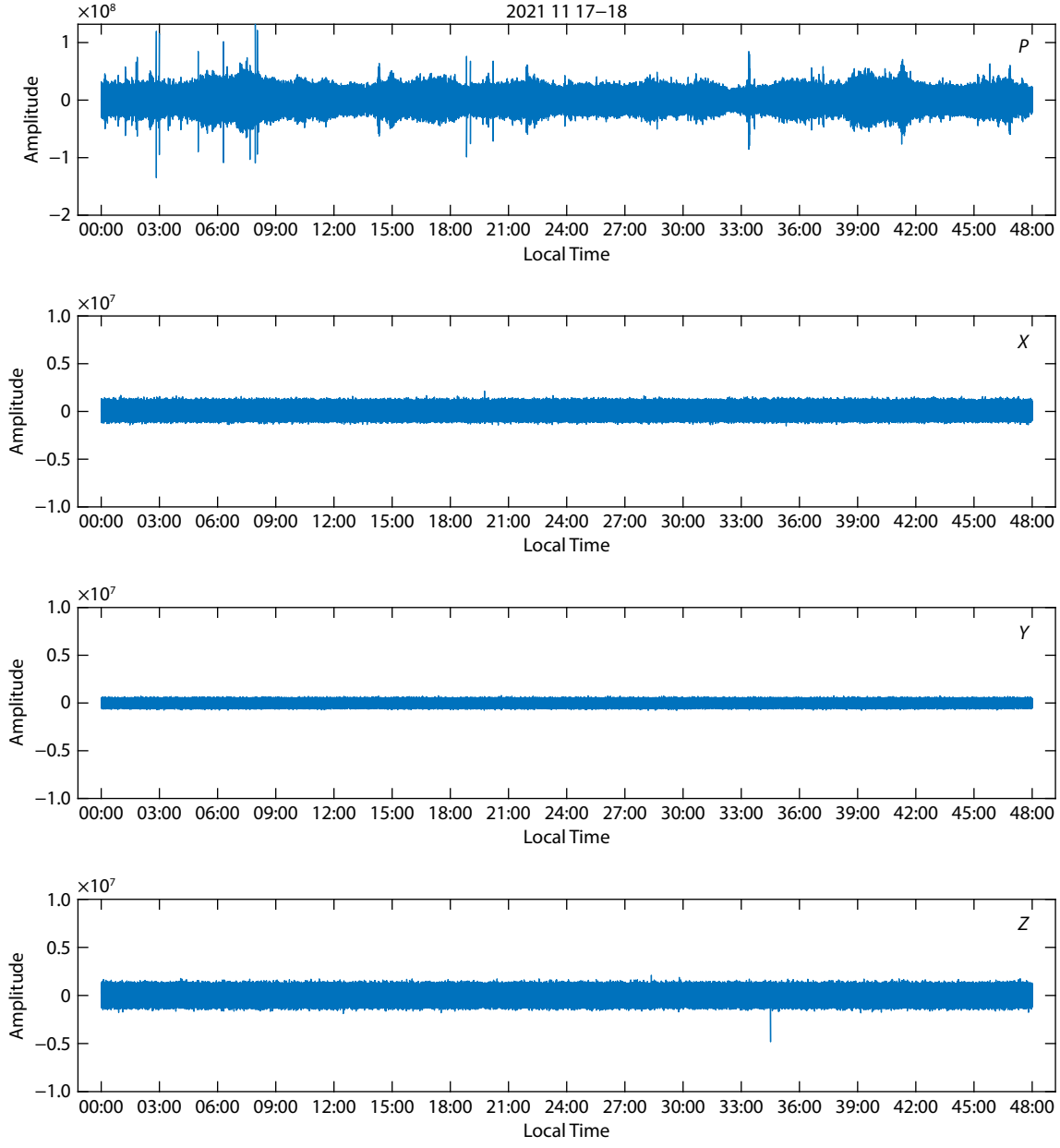

Figure S5. Four-component OBS data of 17/11–18/11. *H* is the data from hydrophone, and *X*, *Y*, *Z* are data from the three geophones.

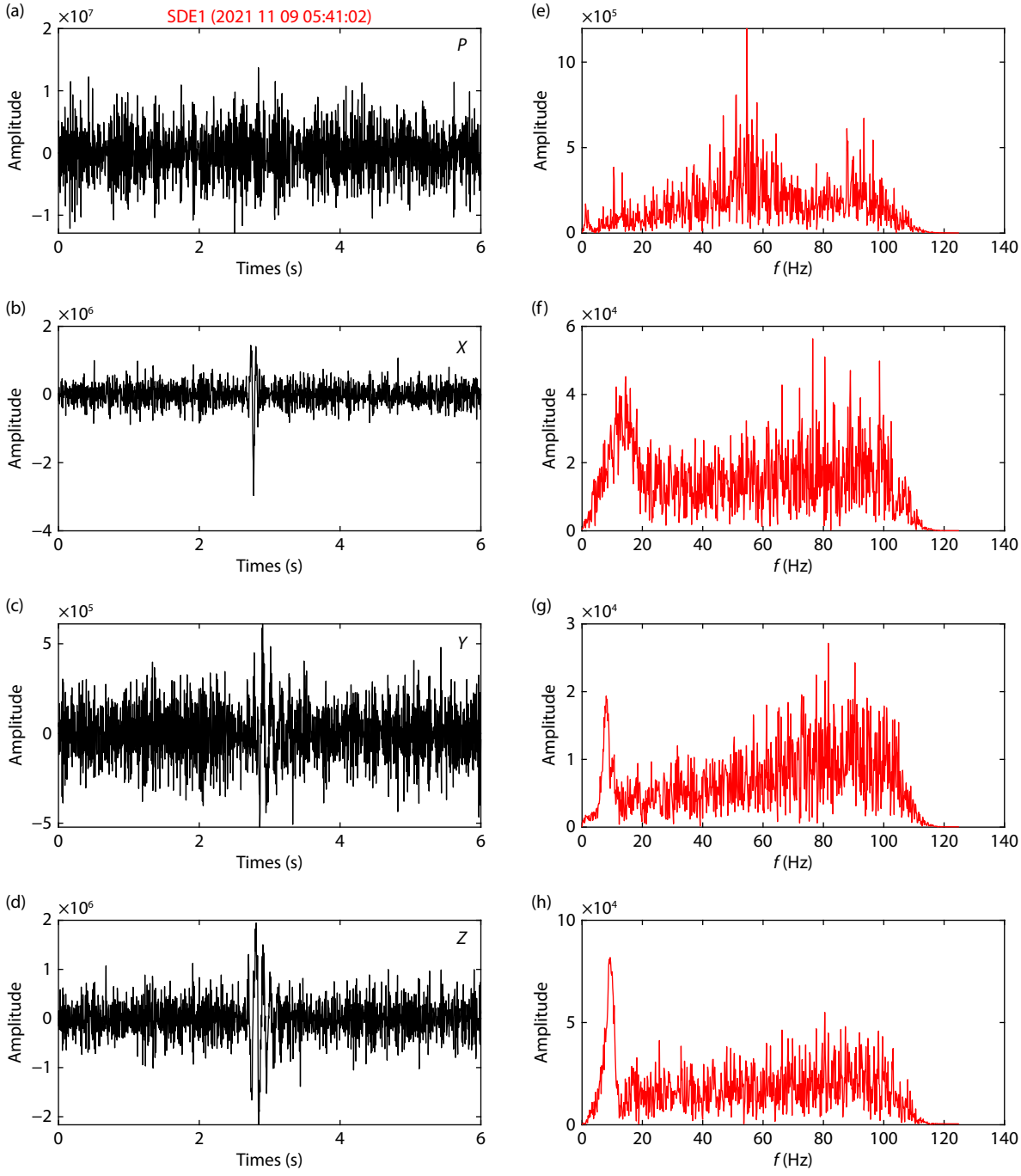

Figure S6. SDE1. (a) and (e) show the hydrophone data and its spectrum. (b) and (f) show the *X* component data and its spectrum. (c) and (g) show the *Y* component data and its spectrum. (d) and (h) show the *Z* component data and its spectrum.

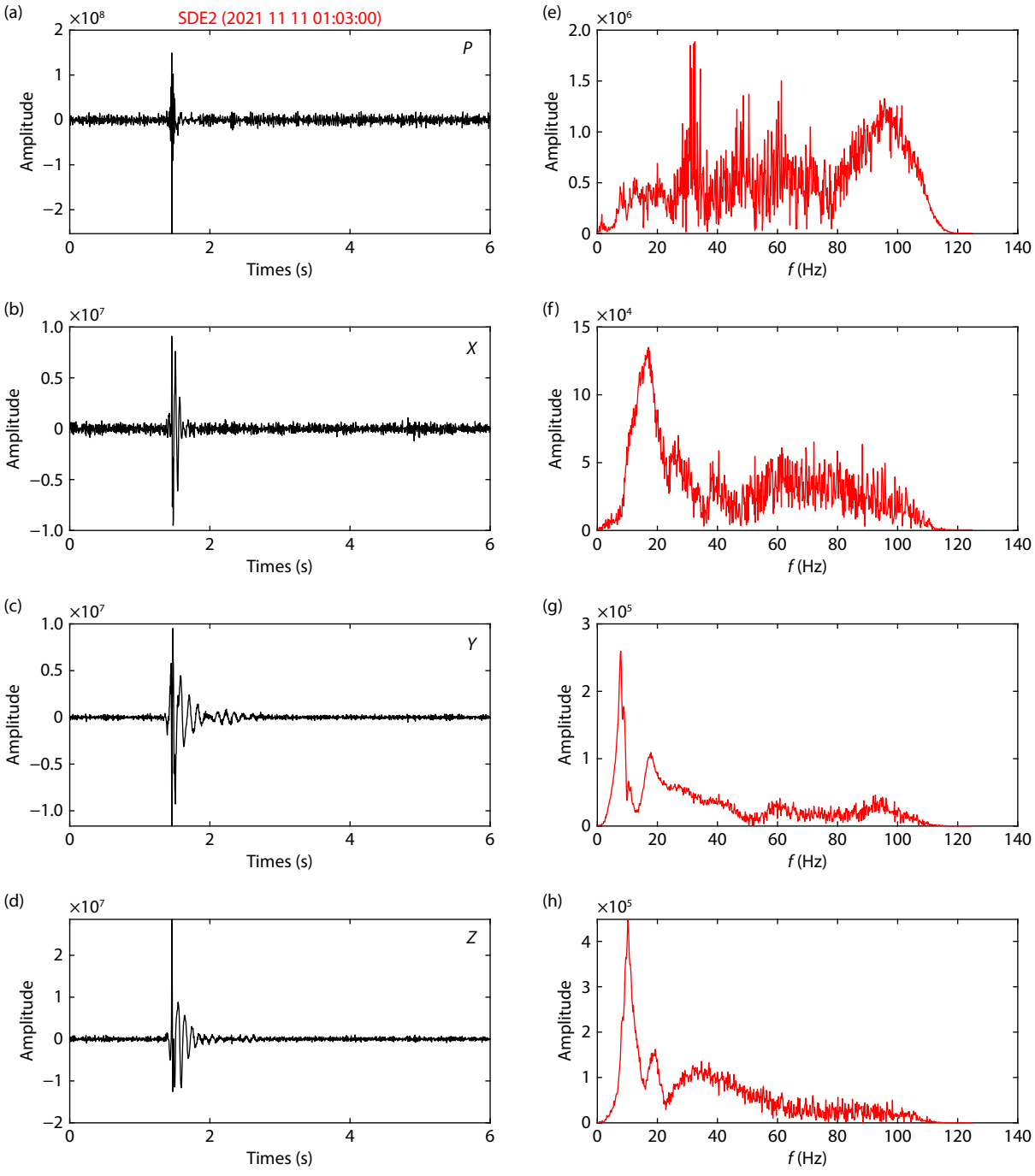

Figure S7. SDE2. (a) and (e) show the hydrophone data and its spectrum. (b) and (f) show the *X* component data and its spectrum. (c) and (g) show the *Y* component data and its spectrum. (d) and (h) show the *Z* component data and its spectrum.

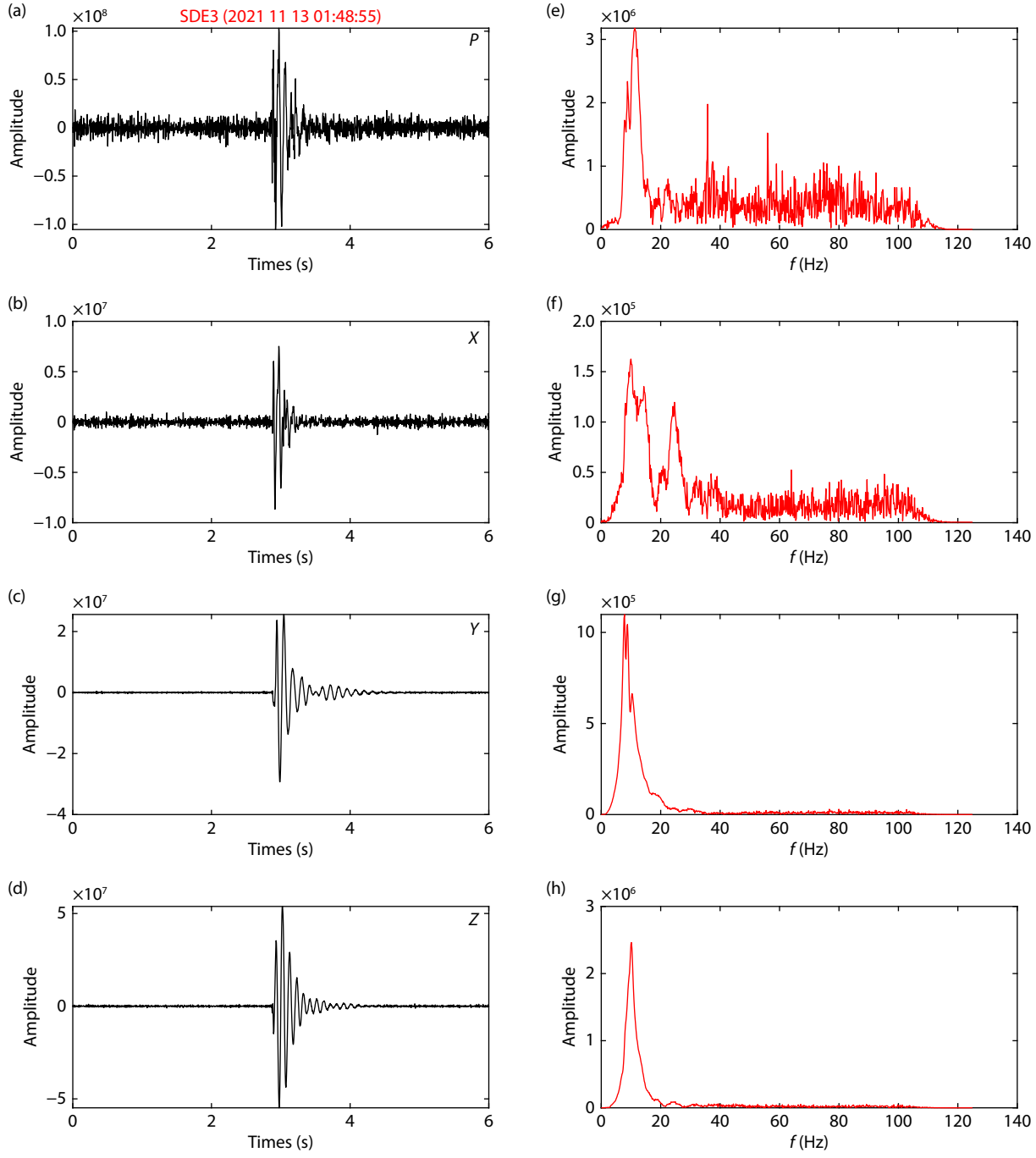

Figure S8. SDE3. (a) and (e) show the hydrophone data and its spectrum. (b) and (f) show the *X* component data and its spectrum. (c) and (g) show the *Y* component data and its spectrum. (d) and (h) show the *Z* component data and its spectrum.

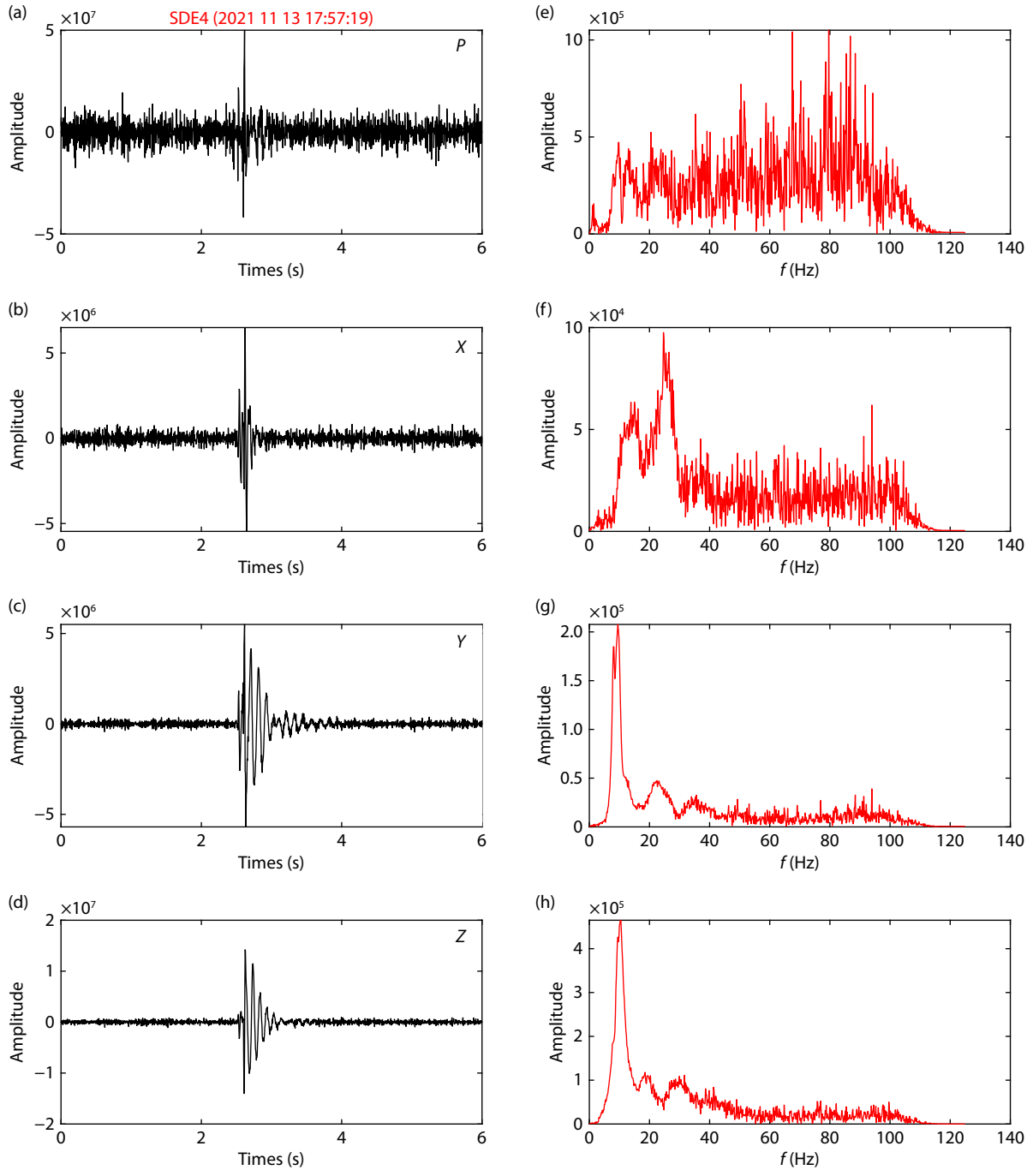

Figure S9. SDE4. (a) and (e) show the hydrophone data and its spectrum. (b) and (f) show the *X* component data and its spectrum. (c) and (g) show the *Y* component data and its spectrum. (d) and (h) show the *Z* component data and its spectrum.

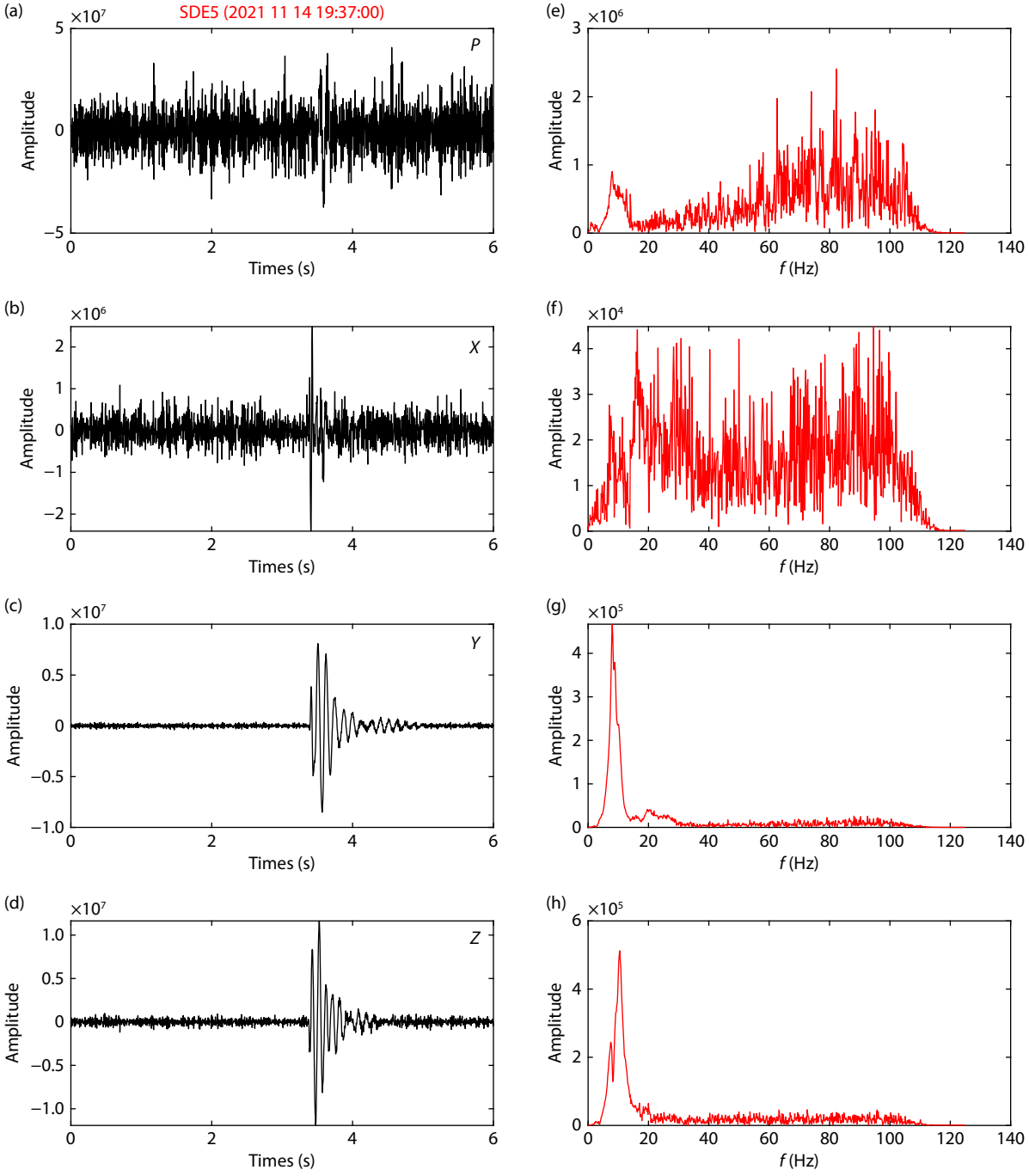

Figure S10. SDE5. (a) and (e) show the hydrophone data and its spectrum. (b) and (f) show the *X* component data and its spectrum. (c) and (g) show the *Y* component data and its spectrum. (d) and (h) show the *Z* component data and its spectrum.